

Title: Morphological Cell Profiling of SARS-CoV-2 Infection Identifies Drug Repurposing Candidates for COVID-19

Running Title: Drug Repurposing Screening for Covid19

Carmen Mirabelli^{1,*}, Jesse W. Wotring^{2,*}, Charles J. Zhang^{2,†}, Sean M. McCarty^{2,†}, Reid Fursmidt^{3,4,†}, Tristan Frum⁵, Namrata S. Kadambi³, Anya T. Amin³, Teresa R. O'Meara¹, Carla D. Pretto¹, Jason R. Spence^{3,5}, Jessie Huang^{6,7}, Konstantinos D. Alysandratos^{6,7}, Darrel N. Kotton^{6,7}, Samuel K. Handelman^{3,4}, Christiane E. Wobus¹, Kevin J. Weatherwax^{4,8,9}, George A. Mashour^{4,8,10}, Matthew J. O'Meara^{11‡}, Jonathan Z. Sexton^{2,3,4,8‡}

¹Department of Microbiology and Immunology, University of Michigan Medical School, Ann Arbor, MI, 48109, USA

²Department of Medicinal Chemistry, College of Pharmacy, University of Michigan, Ann Arbor, MI, 48109, USA

³Department of Internal Medicine, Gastroenterology, Michigan Medicine at the University of Michigan, Ann Arbor, MI, 48109, USA

⁴U-M Center for Drug Repurposing, University of Michigan, Ann Arbor, MI, 48109, USA

⁵Department of Cell and Developmental Biology, University of Michigan, Ann Arbor, MI, 48109, USA

⁶Center for Regenerative Medicine of Boston University and Boston Medical Center, Boston, MA, 02118, USA

⁷The Pulmonary Center and Department of Medicine, Boston University School of Medicine, Boston, MA, 02118, USA.

^aMichigan Institute for Clinical and Health Research (MICHR), University of Michigan, Ann Arbor, MI, 48109, USA
^bCollege of Pharmacy, University of Michigan, Ann Arbor, MI, 48109, USA

⁹College of Pharmacy, University of Michigan, Ann Arbor, MI 48109, USA
¹⁰Department of Anesthesiology, Michigan Medicine at the University of Michigan, Ann Arbor, MI 48109, USA

¹⁰Department of Anesthesiology, Michigan Medicine at the University of Michigan, Ann Arbor, MI, 48109, USA
¹¹Department of Computational Medicine and Bioinformatics, University of Michigan, Ann Arbor, MI, 48109, USA

¹¹Department of Computational Medicine and Bioinformatics, University of Michigan, Ann Arbor, MI, 48109, USA

*These authors contributed equally to this work.

*These authors contributed equally to this work.
†These authors contributed equally to this work.

[†]These authors contributed equally to this work.

Algebra 1

MOI: multiplicity of infection

MOI: multiplicity of infection

COVID-19: Coronavirus Disease

MOA: mechanism of action
IAEGS: integrated approach to gene therapy (IAGT) - IGBTs and other viral vectors

2. *sin*, *sin*, *sin*

The authors declare no conflicts of interest.

Correspondence and requests for materials should be addressed to izsexton@umich.edu.

36 ABSTRACT

37 The global spread of the severe acute respiratory syndrome coronavirus 2 (SARS-CoV-2), and
38 the associated disease COVID-19, requires therapeutic interventions that can be rapidly
39 identified and translated to clinical care. Traditional drug discovery methods have a >90% failure
40 rate and can take 10-15 years from target identification to clinical use. In contrast, drug
41 repurposing can significantly accelerate translation. We developed a quantitative high-
42 throughput screen to identify efficacious agents against SARS-CoV-2. From a library of 1,425
43 FDA-approved compounds and clinical candidates, we identified 17 dose-responsive
44 compounds with *in vitro* antiviral efficacy in human liver Huh7 cells and confirmed antiviral
45 efficacy in human colon carcinoma Caco-2, human prostate adenocarcinoma LNCaP, and in a
46 physiologic relevant model of alveolar epithelial type 2 cells (iAEC2s). Additionally, we found
47 that inhibitors of the Ras/Raf/MEK/ERK signaling pathway exacerbate SARS-CoV-2 infection *in*
48 *vitro*. Notably, we discovered that lactoferrin, a glycoprotein classically found in secretory fluids,
49 including mammalian milk, inhibits SARS-CoV-2 infection in the nanomolar range in all cell
50 models with multiple modes of action, including blockage of virus attachment to cellular heparan
51 sulfate and enhancement of interferon responses. Given its safety profile, lactoferrin is a readily
52 translatable therapeutic option for the management of COVID-19.

53 IMPORTANCE

54 Since its emergence in China in December 2019, SARS-CoV-2 has caused a global pandemic.
55 Repurposing of FDA-approved drugs is a promising strategy for identifying rapidly deployable
56 treatments for COVID-19. Herein, we developed a pipeline for quantitative high-throughput
57 image-based screening of SARS-CoV-2 infection in human cells that led to the identification of
58 several FDA-approved drugs and clinical candidates with *in vitro* antiviral activity.

59 INTRODUCTION

60 SARS-CoV-2 is an enveloped, positive-sense, single-stranded RNA betacoronavirus that
61 emerged in Wuhan, China in November 2019 and rapidly developed into a global pandemic.
62 The associated disease, COVID-19, manifests with an array of symptoms, ranging from flu-like
63 illness and gastrointestinal distress (1, 2) to acute respiratory distress syndrome, heart
64 arrhythmias, strokes, and death (3, 4). Recently, the FDA issued emergency approval of
65 remdesivir, a nucleoside inhibitor prodrug developed for Ebola virus treatment (5). However,
66 there are no established prophylactic strategies or direct antiviral treatments available to limit
67 SARS-CoV-2 infections and to prevent the associated disease COVID-19.

68 Repurposing of FDA-approved drugs is a promising strategy for identifying rapidly deployable
69 treatments for COVID-19. Benefits of repurposing include known safety profiles, robust supply
70 chains, and a short time-frame necessary for development (6). Additionally, approved drugs can
71 serve as chemical probes to understand the biology of viral infection and inform on the
72 molecular targets/pathways that influence SARS-CoV-2 infection. To date, several drug
73 repurposing screening efforts have been reported in various cell systems including non-human
74 primate VeroE6 (7), Huh7.5 (8) and Caco-2 cells (9) with a significant overlap in reported drugs
75 but with wide-ranging potencies. Here, we developed a pipeline for quantitative high-throughput
76 image-based screening of SARS-CoV-2 infection that led to the identification of several FDA-
77 approved drugs and clinical candidates with previously unreported *in vitro* antiviral activity. We
78 also determined that inhibitors of the Ras/Raf/MEK/ERK signaling pathway exhibited proviral
79 activity in Huh7. Mechanism of action studies of lactoferrin, the most promising hit, identified
80 that it inhibits viral attachment, enhances antiviral host cell responses, and potentiates the
81 effects of remdesivir.

82 RESULTS

83 To determine the optimal cell line and assay timing for antiviral drug screening, we assessed
84 SARS-CoV-2 infectivity in Vero E6 (African green monkey kidney cells), Caco-2 (human colon
85 adenocarcinoma cells), Huh7 (human hepatocyte carcinoma cells) and LNCaP (human prostate
86 adenocarcinoma). Viral growth kinetics at a multiplicity of infection (MOI) of 0.2 revealed that
87 each cell line supported viral infection with peak viral titers at 48 hours post infection (hrs p.i.),
88 except for Caco-2, which took 72 hrs (Fig. S1A). The Huh7 cell line was selected for drug
89 screening because it produced the maximum percentage of infected cells (~20%) at 48 hrs p.i.
90 at a MOI of 0.2, while Caco-2 and LNCaP required higher MOI to show the same infection rates
91 (Fig. S1B). Huh7 also exhibited superior signal to background for N protein staining, and viral
92 infection was detectable at an MOI of as low as 0.004 at 48 hrs p.i. (Fig. S1C).

93 **Cell morphological profiling of SARS-CoV-2 infected cells**

94 To gain insight into cellular features that are being perturbed upon infection, a cell painting style
95 morphological profiling assay was developed in 384-well plates. A multiplexed fluorescent dye
96 set labeling the SARS-CoV-2 nucleocapsid protein (N), nuclei (Hoechst 33342), neutral lipids
97 (HCS LipidTox Green), and cytoplasm (HCS CellMask Orange) was used to capture a wide
98 variety of cellular features relevant to viral infectivity, including nuclear morphology, nuclear
99 texture, and cytoplasmic and cytoskeletal features. Cell level features of infected and uninfected
100 cells were measured using a CellProfiler (7) image analysis pipeline. We observed several
101 prominent features associated with SARS-CoV-2 infection, including the formation of syncytia,
102 cytoplasmic protrusions, multiple cell shapes, and positive/negative N protein staining within the
103 nucleus. Fig. 1A shows multiplexed images of infected and uninfected wells and resulting
104 identification/segmentation of infected cells. To systematically explore the morphologies of
105 infected cells, features were dimensionally reduced via the non-linear uniform manifold
106 approximation and projection (UMAP). The analysis showed five regions of interest (ROI) (Fig.
107 1B) with selected phenotypes. These phenotypes included rounded up cells with intense N

108 staining overlapping with the nuclei (ROI I), diffuse N staining in the cytoplasm of cells with
109 normal shape and size (ROI II), and cells with abnormal cytoplasmic protrusions containing
110 punctate N staining (ROI III) or diffused N staining (ROI IV). Most infected cells, however,
111 clustered in syncytia (ROI V), suggesting that infection in Huh7 propagates primarily through
112 cell-to-cell fusion. Fig. 1C shows split violin plots for prominent features that are perturbed in
113 infected vs. uninfected cells. Viral staining, cytoplasmic intensity (CellMask), and nuclear
114 texture all increase in infected cells. In addition, the neutral lipid droplet content increases and
115 the radial distribution of the lipid droplets shifts outwards from the nucleus towards the plasma
116 membrane. Increased lipid accumulation has been observed previously in Hepatitis C virus-
117 infected Huh7 cells (8). The CellMask intensity is increased in infected cells due to the
118 prevalence of syncytia where the disappearance of cell boundaries increases staining intensity
119 at the cell edge. Collectively, our analysis identifies specific features characteristic of SARS-
120 CoV-2 infected cells.

121

122 **Identification of FDA-approved drugs with antiviral activity against SARS-CoV-2**

123 To identify compounds with antiviral activity against SARS-CoV-2, we tested a library of 1,425
124 FDA-approved compounds and rationally included clinical candidates (Supplementary File 1) in
125 Huh7 cells in quantitative high-throughput screening (qHTS) at five concentrations (50 nM, 250
126 nM, 500 nM, 1000 nM and 2000 nM). Compounds were assessed for their antiviral activity
127 (shown schematically in Fig. 2A) using a CellProfiler (7) image analysis pipeline to: 1) identify
128 infected objects in the N protein image (from a single cell to large syncytia), 2) measure their
129 morphologic features, and then 3) tabulate how many nuclei reside within the infected objects to
130 calculate the total percentage of infected cells per well. To increase the accuracy of identifying
131 true actives and decrease the false negative rate of the assay, a liberal selection criteria was

132 employed to choose drugs for follow-up studies (see methods and Fig. 2A). 132 drugs were
133 selected from qHTS screening or by known activity against SARS, MERS or SARS-CoV-2 and
134 carried forward for triplicate dose-response confirmation. Ultimately, 17 dose-responsive
135 compounds were confirmed with IC₅₀ values of less than 1 μM (Fig. 2B and Supplementary
136 Table 1). These compounds include ten that are novel *in vitro* observations (domperidone,
137 entecavir, fedratinib, ipratropium bromide, lactoferrin, lomitapide, metoclopramide, S1RA,
138 thioguanine, and Z-FA-FMK), and seven previously reported (amiodarone, bosutinib, verapamil,
139 gilteritinib, clofazimine (9, 10), niclosamide (11), and Remdesivir(12)). The remaining
140 compounds either lacked efficacy, exhibited cytotoxicity (e.g. Digoxin), or were efficacious only
141 at concentrations above 1 μM (e.g. hydroxychloroquine, chloroquine) and were thus not
142 prioritized for follow-up. Collectively, the 17 identified hits could be stratified by compound class
143 as ion channel modulators (amiodarone, verapamil, clofazimine, and S1RA), nucleosides/DNA
144 binders (remdesivir, entecavir, niclosamide, and thioguanine), kinase inhibitors (bosutinib,
145 fedratinib, and gilteritinib) and others (Table 1).

146

147 **Hit validation in Caco-2, LNCaP, Vero E6 and an iPSC-derived model of alveolar epithelial
148 cells, the iAEC2.**

149 To evaluate the translatability of the 17 hits from Huh7 cells in other cell systems, we confirmed
150 activity in LNCaP, Caco-2, and Vero E6 cell lines and in physiologically-relevant iPSC-derived
151 alveolar epithelial type 2 cells (iAEC2s) (13). Antiviral activities across the cell systems are
152 shown in Table 1. iAEC2s were used as a biomimetic model of the human bronchial epithelium
153 that is involved in COVID-19 pathogenesis (14). iAEC2s are permissive to SARS-CoV-2
154 infection, exhibiting 10-20% N protein-positive cells at MOI of 0.2 and 50-60% positivity at MOI
155 of 10. Upon infection, we observed long tubular protrusions that co-stained with viral N protein

156 (Fig. 3A). Additionally, unlike the Huh7 model, the vast majority of infected iAEC2 cells were not
157 present in viral syncytia, suggesting that cell-to-cell spread by cell fusion is limited in this model.
158 Nine out of the 17 hits -amiodarone, lomitapide, ipratropium bromide, gilteritinib, fedratinib, and
159 clofazimine, remdesivir, S1RA and bovine lactoferrin- showed dose-responsive antiviral activity
160 against SARS-CoV-2 in iAECs (Table 1). Remarkably, even at a high MOI of 10, bovine
161 lactoferrin, human lactoferrin, S1RA, and remdesivir ($IC_{50} = 18 \text{ nM}$) retained antiviral activity,
162 reflecting the strong efficacy of these compounds in virus-saturated infection conditions (Fig.
163 3B). Six compounds (Amiodarone, Ipatropium Bromide, Lactoferrin, Lomitapide, Remdesivir, Z-
164 FA-FMK) maintained efficacy across all tested cell systems (Table 1), suggesting the targets are
165 conserved across multiple cell types.

166 **Characterization of antiviral hits and identification of compounds that exacerbate viral
167 infection.**

168 To stratify compounds, we performed a time-of-addition study with compound added either 4 hrs
169 prior to infection (as done previously in the screen) or 1 hr p.i. (Fig. 4A). We infected Huh7 with
170 SARS-CoV-2 at MOI of 1 and then quantified infection by detecting the positive-strand viral RNA
171 genome by RNAscope (Fig 4B). We found that verapamil, entecavir, and niclosamide lost
172 activity under these experimental conditions (Fig. 4C). Amiodarone, clofazimine, S1RA,
173 lomitapide, Z-FA-FMK, the other nucleoside analogues remdesivir and thioguanine, and the
174 kinase inhibitors bosutinib, fedratinib, and gilteritinib retained activity regardless of compound
175 addition pre- or post-infection, suggesting that they inhibit post-binding entry events. Two
176 compounds, ipratropium bromide and metoclopramide, lost activity when added 1 hr p.i.,
177 suggesting a role in viral binding inhibition. Although they share the same molecular target
178 (dopamine D2 receptor), metoclopramide and domperidone seem to exert their antiviral activity
179 with different modes of action, either by directly inhibiting binding or indirect effects on the host.

180 Our screening also identified compounds that exacerbated infection. All Mitogen/Extracellular
181 signal-regulated Kinase (MEK) inhibitors tested (cobimetinib, trametinib, and binimatinib)
182 resulted in a >2-fold increase of viral infection in Huh7 (Fig. 5A, B). To confirm this finding, we
183 performed RNAscope on virus-infected, cobimetinib-treated versus untreated cells 24 and 48
184 hrs p.i. (Fig. 5C). The percentage of viral RNA-positive cells was increased at 48 hrs p.i., but not
185 at 24 hrs p.i., following treatment, suggesting that these compounds could enhance virus
186 spread. In addition, upon treatment with the three MEK inhibitors, and cobimetinib in particular,
187 we observed an increased syncytia size (Fig 5A) and different patterns of localization of viral
188 RNA and S protein within the infected cells (Fig 5C). These immunofluorescence staining
189 patterns suggest a difference in viral compartmentalization and spread in MEK inhibitor-treated
190 cells. The increased infection and the diffuse localization of viral RNA was recapitulated when
191 treating the cells with a molecular probe, U0126 (10 µM), that is commonly used as an inhibitor
192 of the Ras-Raf-MEK-ERK pathway. Taken together, these data highlight the utility of screening
193 FDA-approved compounds as a way of identifying cellular pathways involved in viral infection.

194

195 **Lactoferrin blocks SARS-CoV-2 replication at different stages of the viral cycle.**

196 The most broadly efficacious hit identified was lactoferrin, a protein found in colostrum and
197 airway epithelium (15). To confirm our previous finding of inhibition of N protein expression by
198 lactoferrin, we infected Huh7 cells with SARS-CoV-2 (MOI of 0.2) under increasing doses of
199 lactoferrin and measured viral RNA using RT-qPCR at 48 hrs p.i. (Fig. 6A). Lactoferrin exhibited
200 a dose-dependent inhibition of viral replication (Fig. 6A) and retained antiviral activity through a
201 range of MOIs (Fig. 6B). It maintained antiviral activity even when added 1 or 24 hrs after
202 infection, suggesting multiple modes of antiviral action (Fig. 6B). Previous work on lactoferrin in
203 the context of SARS-CoV-1 suggested that lactoferrin blocks viral entry by binding heparan

204 sulfate proteoglycans, which are viral attachment factors (16). Therefore, we performed a viral
205 binding assay by incubating SARS-CoV-2 (MOI of 10) in the presence of lactoferrin (1250 nM
206 and 6250 nM) for one hour on ice followed by quantification of viral RNA by RT-qPCR (Fig. 6C).
207 Remdesivir was included as a negative control as it blocks viral infection at a post-binding step.
208 Both concentrations of lactoferrin, but not remdesivir, blocked SARS-CoV-2 attachment to Huh7
209 cells (Fig. 6C). As a positive control, Huh7 cells were treated with NaClO₃, a protein sulfation
210 inhibitor that depletes cells of heparan sulfate (17). SARS-CoV-2 binding to cells was reduced
211 in NaClO₃-treated cells, and additional lactoferrin treatment did not further reduce binding (Fig.
212 6C). These data suggest that, similar to SARS-CoV-1, lactoferrin blocks viral attachment via
213 neutralizing heparan sulfate proteoglycans. Another potential mechanism of action of lactoferrin
214 is through enhancement of interferon responses, which can then limit viral replication within host
215 cells (18). We therefore evaluated mRNA levels of IFN β and the interferon-stimulated genes
216 ISG15, MX1, Viperin and IFITM3 in lactoferrin-treated Huh7 cells (Fig. 6D). SARS-CoV-2
217 infection did not result in a robust interferon response consistent with previous studies (19).
218 However, we did detect an upregulation of IFN β and ISG transcripts in virus-infected and
219 lactoferrin-treated cells, suggesting that the post-entry antiviral activity of lactoferrin is interferon-
220 mediated. To rule out iron chelation as a potential mode of action, iron-saturated hololactoferrin
221 and transferrin were tested in Huh7 cells; the former retained activity and the latter was inactive
222 (Fig. 6E). Given the pronounced single-agent efficacy of lactoferrin, we further tested whether
223 combinations with the FDA-approved agent remdesivir could improve the overall antiviral
224 activity. We found that lactoferrin potentiated the efficacy of remdesivir 8-fold (Fig. 6F),
225 suggesting that lactoferrin could be beneficial in the management of COVID-19 both as a single
226 agent or in combination.

227

228 **DISCUSSION**

229 In this study, we developed an experimental workflow based on high-content imaging and
230 morphological profiling that allows for rapid screening of FDA-approved compounds, and
231 identified 17 compounds that inhibit SARS-CoV-2 infection *in vitro*. Of these, seven were
232 previously reported and serve as a benchmark validation of our endpoints and experimental
233 approach, and ten were hitherto unknown. We evaluated the antiviral activity of the 17 hits
234 identified in Huh7 in three transformed cell lines (VeroE6, Caco-2, and LNcaP) and one non-
235 transformed cell line (iAECs) and observed six compounds (amiodarone, ipratropium bromide,
236 lactoferrin, lomitapide, remdesivir, Z-FA-FMK) exhibiting activity across multiple cell lines.

237 Since the completion of this study (June 2020), over 30 studies reporting SARS-CoV-2 antiviral
238 activity of FDA-approved drugs have been published. A meta-analysis of these *in vitro* screens
239 (including this effort) show consensus around 11 compounds, with small total overlap between
240 studies (20). This observation suggests that drug screening of FDA-approved compounds is
241 highly dependent on the chosen cell line and infection conditions. It is expected that
242 compounds exerting an antiviral effect through direct binding to viral proteins would be more
243 independent of the chosen cell system rather than drugs modulating host cell factors that can
244 vary widely. For example, we observed conservation of activity across cell systems for
245 remdesivir, which directly inhibits the viral polymerase (21), and also for lomitapide, which is
246 proposed to directly inhibit recombinant SARS-CoV-2 main protease (Mpro)(22).

247 As most FDA-approved drugs are optimized against human molecular targets, active
248 compounds can lead to target identification of host factors involved in SARS-CoV-2 infection. Z-
249 FA-FMK is an irreversible cathepsin L inhibitor that exhibits potent antiviral activity in all of the
250 five cell systems tested herein, presumably because cathepsin L has been shown to be an entry
251 factor of SARS-CoV-2 (23, 24). Another hit in our Huh7 screen, fedratinib, was approved by the
252 FDA in 2019 for myeloproliferative neoplasms (25) and is an orally bioavailable semi-selective
253 JAK1/JAK2 inhibitor. JAK inhibitors have been proposed for COVID-19 treatment to specifically

254 inhibit Th17-mediated inflammatory response (26, 27) and to block numb-associated kinase
255 responsible for clathrin-mediated viral endocytosis (28). The JAK inhibitor baricitinib (29) in
256 combination with remdesivir was recently granted emergency use authorization by the FDA,
257 while jakotinib ([ChiCTR2000030170](#)), and ruxolitinib ([ChiCTR2000029580](#)) are currently being
258 evaluated in clinical trials for COVID-19 as potential dual action therapeutics (antiviral and
259 innate immune response).

260 In contrast to the antiviral drug hits, all FDA-approved MEK inhibitors tested exacerbated viral
261 infection, likely by increasing cell-to-cell spread as suggested by the formation of larger syncytia
262 and more diffuse localization of viral RNA and S protein within infected cells (Fig. 5). Intriguingly,
263 in the context of other virus infections, including SARS-CoV-1, pharmacological inhibition of the
264 Ras-Raf-MEK-ERK pathway results in restriction of viral infection (30). This underscores the
265 importance of this pathway during viral infections and warrants further examination into the
266 mechanism of action of this signaling cascade during SARS-CoV-2 infection.

267 This study has generated several clinically testable and readily translatable hypotheses. As an
268 example, we observed potent antiviral activity of ipratropium bromide (Atrovent), a quaternary
269 ammonium salt and muscarinic receptor antagonist that is commonly prescribed for asthma. It is
270 administered via inhalation into the lungs with little systemic absorption. Given its potential
271 mode of action as inhibitor of SARS-CoV-2 attachment, prophylaxis or post-exposure treatment
272 with ipratropium bromide may curb infection of the upper respiratory tract and drastically reduce
273 systemic viral spread and development of severe symptoms while achieving beneficial
274 bronchodilation. Similarly, we identified metoclopramide and domperidone, both dopamine D2
275 receptor antagonists used to treat gastrointestinal symptoms, as SARS-CoV-2 inhibitors.
276 Gastrointestinal symptoms have been increasingly reported in more than half of the patients
277 infected by SARS-CoV-2 (2). Hence, these compounds may ameliorate GI symptoms during

278 COVID-19 infection, and in addition the reduced viral load in the GI tract could also reduce
279 fecal-oral transmission of SARS-CoV-2 (31).

280 Most noteworthy, our screen identified bovine lactoferrin, a safe and widely available dietary
281 supplement, with multi-modal efficacy in multiple cell systems, including non-transformed and
282 physiologically relevant iAEC2s. Lactoferrin gene expression was shown to be highly
283 upregulated in response to SARS-CoV-1 infection (32) and, in addition to enhancing natural
284 killer cell and neutrophil activity, lactoferrin blocks SARS-CoV-1 attachment through binding to
285 heparan sulfate proteoglycans (15). Here, we showed that lactoferrin has a multi-modal
286 mechanism of action against SARS-CoV-2 infection (Fig. 6). First, it strongly inhibits cellular
287 binding of SARS-CoV-2 to cells via competition with heparan sulfate. Second, it retains antiviral
288 efficacy at 24 hrs p.i. and it modulates host cell immunity through increased expression of
289 interferon and several interferon-stimulated genes. Through heightening the innate immune
290 response of host cells, orally administered lactoferrin could be especially effective in resolving
291 the gastrointestinal symptoms that are present in COVID-19 patients (33) with a mechanism
292 similar to norovirus infection (34). In addition, lactoferrin was previously shown to decrease the
293 production of IL-6 (35), which is one of the key players of the “cytokine storm” produced by
294 SARS-CoV-2 infection (36, 37). Lactoferrin is classified by the FDA as ‘Generally Recognised
295 as Safe’ (GRAS) and therefore may represent a promising therapy for pre- and post-exposure
296 prophylaxis.

297 Combination therapies are likely to be required for effectively treating SARS-CoV-2 infection,
298 and this approach has already shown promise, i.e., combination therapy with interferon β -1b,
299 lopinavir–ritonavir, and ribavirin showed efficacy against SARS-CoV-2 in a prospective, open-
300 label, randomized, phase 2 trial (38). Here, we show that lactoferrin potentiates the antiviral
301 activity of remdesivir and could be used in combination therapy with these drugs, which are
302 currently being used or studied for the treatment of COVID-19. Due to its wide availability,

303 limited cost, and strong safety profile, lactoferrin could be a rapidly deployable option for both
304 prophylaxis and the management of COVID-19. Although our findings are promising, further
305 studies are needed to confirm the efficacy of our lead antiviral compounds in animal models
306 and/or clinical studies.

307

308 **METHODS**

309 **Cells and virus.**

310 Vero E6, Caco-2, LNcaP and Huh7 cells were maintained at 37°C with 5% CO₂ in Dulbecco's
311 Modified Eagle's Medium (DMEM; Welgene), supplemented with 10% heat-inactivated fetal
312 bovine serum (FBS), HEPES, non-essential amino-acids, L-glutamine and 1X Antibiotic-
313 Antimycotic solution (Gibco). iPSC (SPC2 iPSC line, clone SPC2-ST-B2, Boston University)
314 derived alveolar epithelial type 2 cells (iAEC2s) were differentiated and maintained as
315 alveolospheres embedded in 3D Matrigel in "CK+DCI" media, as previously described (Jacob et
316 al. 2019). iAEC2s were passaged approximately every two weeks by dissociation into single
317 cells via the sequential application of dispase (2 mg/ml, Thermo Fisher Scientific, 17105-04) and
318 0.05% trypsin (Invitrogen, 25300054) and re-plated at a density of 400 cells/µl of Matrigel
319 (Corning, 356231), as previously described (39). SARS-CoV-2 WA1 strain was obtained by BEI
320 resources and was propagated in Vero E6 cells. Lack of genetic drift of our viral stock was
321 confirmed by deep sequencing. Viral titers were determined by TCID₅₀ assays in Vero E6 cells
322 (Reed and Muench method) by microscopic scoring. All experiments using SARS-CoV-2 were
323 performed at the University of Michigan under Biosafety Level 3 (BSL3) protocols in compliance
324 with containment procedures in laboratories approved for use by the University of Michigan
325 Institutional Biosafety Committee (IBC) and Environment, Health and Safety (EHS).

326 **Viral titer determination.**

327 Vero E6, Caco-2, LNCaP and Huh7 cells were seeded in a 48-well plate at 2×10^4 cells/well and
328 incubated overnight at 37°C with 5% CO₂. Cells were then infected with SARS-CoV-2 WA1 at a
329 multiplicity of infection (MOI) of 0.2. One hour after infection, cells were harvested (day 0 of
330 infection) or kept at 37°C for 1, 2 and 3 days p.i.. Viral titer determination was performed by
331 TCID₅₀ assay on Vero E6 cells of the total virus (supernatant and intracellular fraction).
332 Alternatively, cells were harvested with Trizol and total cellular and viral RNA was extracted with
333 the ZymoGen Direct-zol RNA extraction kit. Viral RNA was quantified by RT-qPCR using the
334 2019-nCoV CDC qPCR Probe Assay and the probe set N1 (IDT technologies). IFNβ, viperin,
335 MX1, ISG15, IFITM3 and the housekeeping gene GAPDH mRNA levels were quantified by
336 qPCR with SsoAdvanced™ Universal SYBR® Green Supermix (Bio-Rad) with specific primers
337 (IFNβ: F-TTGACATCCCTGAGGAGATTAAGC, R- TCCCACGTACTCCAACTTCCA; MX1: F-
338 CCAGCTGCTGCATCCCACCC, R-AGGGGCGCACCTT CTCCTCA; ISG15: F-
339 TGGCGGGCAACGAATT, R- GGGTGATCTGCGCCTTCA; IFITM3: F-TCCCAC
340 GTACTCCAACTTCCA, R-AGCACCAGAAACACGTGCACT; GAPDH: F-
341 CTCTGCTCCTCGAC, R-GCGCCCCACCAAGCTCAAGA). Fold increase was
342 calculated by using the ΔΔC_t method over non-infected and untreated Huh7.

343 **Viral infectivity assay.**

344 384-well plates (Perkin Elmer, 6057300) were seeded with Huh7 cells at 3000 cells/well and
345 allowed to adhere overnight. Compounds were then added to the cells and incubated for 4
346 hours. The plates were then transferred to BSL3 containment and infected with SARS-CoV-2
347 WA1 at a multiplicity of infection (MOI) of 0.2 in a 10 μL addition with shaking to distribute virus.
348 For the final dose-responses curves, porcine trypsin (Sigma-Aldrich, T0303) at a final
349 concentration of 2 μg/ml was included during infection. After one hour of absorption, the virus

350 inoculum was removed and fresh media with compound was added. Uninfected cells and
351 vehicle-treated cells were included as positive and negative control, respectively. Two days
352 post-infection, cells were fixed with 4% PFA for 30 minutes at room temperature, permeabilized
353 with 0.3% Triton X-100, and blocked with antibody buffer (1.5% BSA, 1% goat serum and
354 0.0025% Tween 20). The plates were then sealed, surface decontaminated, and transferred to
355 BSL2 for staining with the optimized fluorescent dye-set: anti-nucleocapsid protein (anti-NP)
356 SARS-CoV-2 antibody (Antibodies Online, Cat# ABIN6952432) overnight treatment at 4 °C
357 followed by staining with secondary antibody Alexa-647 (goat anti-mouse, Thermo Fisher,
358 A21235), Hoechst-33342 pentahydrate (bis-benzimide) for nuclei staining (Thermo Fisher,
359 H1398), HCS LipidTOX™ Green Neutral Lipid Stain (Thermo Fisher, H34475), and HCS
360 CellMask™ Orange for cell delineation (Thermo Fisher H32713). iAEC2 maintained in 3D
361 culture were dissociated to single cells and seeded in collagen coated 384-well plates at a
362 seeding density of 8000 cells/well in the presence of 10 µM Y-27632 for the first 72 hours after
363 plating (APExBIO, A3008) to grow to roughly 80% confluence. Infection was performed at MOI
364 of 10 in the presence of 2 µg/ml of trypsin porcine (Sigma-Aldrich, T0303). Staining protocol for
365 the iAEC2s differed slightly with the addition of an anti-acetylated tubulin primary antibody (Cell
366 Signaling, 5335), instead of HCS CellMask Orange, and the use of an additional secondary
367 Alexa 488 antibody (donkey anti-rabbit, Jackson ImmunoResearch, 711-545-152).

368 **Compound library.**

369 The compound library deployed for drug screening was created using the FDA-Approved Drugs
370 Screening Library (Item No. 23538) from Cayman Chemical Company. This library of 875
371 compounds was supplemented with additional FDA approved drugs and selected clinical
372 candidates from other vendors including MedChemExpress, Sigma Aldrich, and Tocris. Clinical
373 candidates and chemical probes were included if they had any reported antiviral efficacy or had
374 an association with SARS1, MERS or SARS-CoV-2. The library was formatted in five 384-well

375 compound plates and was dissolved in DMSO at 10 mM. Hololactoferrin (Sigma Aldrich,
376 L4765), apolactoferrin (Jarrow Formulas, 121011), native human lactoferrin (Creative BioMart,
377 LFT-8196H), and transferrin (Sigma Aldrich, T2036) were handled separately and added
378 manually in cell culture media. Dilution plates were generated for qHTS at concentrations of 2
379 mM, 1 mM, 500 µM, 250 µM and 50 µM and compounds were dispensed at 1:1000 dilution.

380 **qHTS primary screen and dose response confirmation.**

381 For the qHTS screen, compounds were added to cells using a 50 nL pin tool array on a Caliper
382 Life Sciences Sciclone ALH 3000 Advanced Liquid Handling system. Concentrations of 2 µM, 1
383 µM, 500 nM, 250 nM and 50 nM were included for the primary screen. In all dose-response
384 confirmation experiments, compounds were dispensed using an HP D300e Digital Compound
385 Dispenser and normalized to a final DMSO concentration of 0.1% DMSO. Dose response
386 confirmation was performed in triplicate and in 10-point:2-fold dilution. Z-primes for dose
387 response plates ranged between 0.4-0.8.

388 **Imaging.**

389 Stained cell plates were imaged on both Yokogawa CQ1 and Thermo Fisher CX5 high content
390 microscopes with a 20X/0.45NA LUCPlan FLN objective. Yokogawa CQ1 imaging was
391 performed with four excitation laser lines (405nm/488nm/561nm/640nm) with spinning disc
392 confocal and 100ms exposure times. Laser power was adjusted to yield optimal signal to noise
393 ratio for each channel. Maximum intensity projection images were collected from 5 confocal
394 planes with a 3-micron step size. Laser autofocus was performed and nine fields per well were
395 imaged covering approximately 80% of the well area. The Thermo Fisher CX5 with LED
396 excitation (386/23nm, 485/20nm, 560/25nm, 650/13nm) was also used and exposure times
397 were optimized to maximize signal/background. Nine fields were collected at a single Z-plane as

398 determined by image-based autofocus on the Hoechst channel. The primary qHTS screen was
399 performed using CX5 images and all dose-response plates were imaged using the CQ1.

400 **Image segmentation and feature extraction and infection score.**

401 The open source CellProfiler software (12) was used in an Ubuntu Linux-based distributed
402 Amazon AWS cloud implementation for segmentation, feature extraction, infection scoring and
403 results were written to an Amazon RDS relational database using MySQL. A pipeline was
404 developed to automatically identify infected cells in a field and to enable cell-level morphologic
405 profiling. Infected areas were identified by Otsu thresholding and segmentation using the N-
406 protein image, then all nuclei were identified in a similar manner in the Hoechst-33342 image,
407 and the “relate objects” module was used to relate nuclei to an infected cell area. If a nucleus
408 was found to reside within an infected area, then it and its corresponding cell area was labeled
409 “infected”. The percentage of infected cells was tabulated by dividing the infected cell number
410 by the total cell number summed across all 9 fields per well. To enable morphologic cell
411 profiling, the following regions of interest were defined for feature extraction: nuclei, cell,
412 cytoplasm, nucleoli, neutral lipid droplets and syncytia. Multiple intensity features and radial
413 distributions were measured for each object in each channel and cell size and shape features
414 were measured. Nuclei were segmented using the Hoechst-33342 image and the whole cell
415 mask was generated by expanding the nuclear mask to the edge of the Cell Mask Orange
416 image. Plate-based normalization was performed to account for variability in infection
417 percentage. The assay window was normalized between the positive control wells (32
418 uninfected wells representing 0% inhibition) and the negative control wells (32 infected
419 wells, 0.1% DMSO vehicle treated representing 100% effect). The compound treated wells
420 were scored with the RF model and the efficacy score was normalized to the individual
421 plate.

422 **Data pre-processing.**

423 Cell level data were pre-processed and analyzed in the open source Knime analytics platform
424 (39). Cell-level data was imported into Knime from MySQL, drug treatment metadata was
425 joined, and features were centered and scaled. Features were pruned for low variance (<5%)
426 and high correlation (>95%) and resulted in 660 features per cell.

427 **Statistical methods and hypothesis testing.**

428 Dose-response curves were fit and pairwise differences between experimental conditions
429 were tested using Prism (Graphpad Software, San Diego, CA, USA). Other statistical tests
430 including non-parametric Mann-Whitney were performed in the statistical programming
431 language and environment R.

432 **UMAP embedding.**

433 The embed_umap application of MPLearn (v0.1.0, <https://github.com/momeara/MPLearn>) was
434 used to generate UMAP embeddings. Briefly, for a set of cells, each feature was per-plate
435 standardized and jointly orthogonalized using sklearn.IncrementalPCA(n_components=379,
436 batch_size=1000). Then, features were embedded into 2 dimensions using umap-learn
437 (v0.4.1)(41). UMAP(n_components=2, n_neighbors=15, min_dist=0, init='spectral',
438 low_memory=True). Embeddings were visualized using Holoviews Datashader (v1.12.7) (42),
439 using histogram equalization and the viridis color map.

440 **Data analytics.**

441 HC Stratominer (Core Life Analytics, Utrecht NL) was used as an independent method for hit-
442 calling and performs fully automated/streamlined cell-level data pre-processing and score
443 generation. IC Stratominer was also used to fit dose response curves for qHTS. Compound

444 registration and assay data registration were performed using the open source ACAS
445 platform (Refactor BioSciences github <https://github.com/RefactorBio/acas>).

446 **Dose-response analysis and compound selection.**

447 In qHTS screening, a compound was selected to be carried forward into dose response
448 confirmation when meeting one of the following criteria: 1) Percent infected less than 25% for
449 the median field in at least two concentrations, 2) a dose-response relationship was observed
450 (by inspection) across the five concentrations tested, or 3) compounds of interest not meeting
451 this criteria were carried forward if reported positive in the literature or were being evaluated in
452 clinical trials for COVID-19.

453 **Dose response analysis in the confirmation and combinatorial screening.**

454 Due to the spatial inhomogeneity of infected cells across a single well, approximately half of the
455 fields were undersaturated, resulting in a reproducible distribution per-well. Total cell and
456 infected cell counts were summed over the 9 fields and percent infected cells was averaged
457 over triplicate wells. Cells treated with known fluorescent compounds, including Clofazimine,
458 were confirmed to not have spectral interference. Dose response curves were fit with Graphpad
459 Prism using a semilog 4-parameter variable slope model.

460 **Viral Binding assay.**

461 Huh-7 cells were plated in 48-well plates at 100,000 cells per well and allowed to adhere
462 overnight. The following day, compounds were added at the indicated concentration in serum-
463 free DMEM and incubated for 1 hour at 4 °C. Following compound incubation, cells were
464 infected with SARS-CoV-2 at an MOI of 10 for 1 hour at 4 °C to allow for viral binding. Cells were
465 then washed 3 times with ice cold PBS to remove unbound virus and RNA was extracted by
466 using the Direct-Zol RNA miniprep kit (Zymogen, R2052). Bound virus was then quantified by

467 RT-qPCR (see section Viral titer determination and host gene quantification) and percentages
468 were calculated over the infected non-treated condition.

469 **Multi-cycle cytopathogenic effect (CPE) reduction assay.**

470 Vero E6 were allowed to adhere overnight in 96-well cell culture plates. A 2-fold 10-point serial
471 dilution of compounds (5000 nM-5 nM) and SARS-CoV-2 at MOI of 0.002 were added. CPE
472 was evaluated by microscopic scoring at 5 d.p.i. The 50% inhibitory concentration (IC₅₀) was
473 calculated by logarithmic interpolation and is defined as the concentration at which the virus-
474 induced CPE is reduced by 50%.

475 **RNAscope of SARS-CoV-2 infected cells.**

476 PFA-fixed 96-well black plates (Corning, cat nr. 3036) were permeabilized with a step-wise
477 EtOH treatment (25% EtOH for 3 minutes, 50% EtOH for 3 minutes and 70% EtOH
478 overnight at 4 °C). The day after, cells were treated with washing buffer (25% formamide in
479 1X SSC buffer) for 5 minutes and hybridized with custom-designed probes targeting
480 positive-sense SARS-CoV-2 RNA directly conjugated with ATTO647 (Ann Arbor
481 Bioscience) at 37 °C overnight in hybridization buffer (dextran sulfate, 25% formamide and
482 0.1 % SDS). Cells were counterstained with Hoechst 33342 and anti-S protein antibody (Spike
483 antibody 1A9, GeneTex, Cat Nr. GTX632604) and imaged using a Thermo Fisher CX5 high
484 content microscope with a 10X/0.45NA LUCPlan FLN objective.

485

486 **ACKNOWLEDGEMENTS**

487 Funding: University of Michigan Institute for Clinical and Health Research (MICHR) (NCATS -
488 UL1TR002240) and its Center for Drug Repurposing. JZS is supported by the National Institute

489 of Diabetes and Digestive and Kidney Diseases (R01DK120623). JWW is supported by the
490 pharmacological sciences training program (PSTP) T32 training grant. CM is supported by
491 Marie-Sladowska Curie individual fellowship (GA - 841247) and MICHR Postdoctoral
492 Translational Scholars Program. KDA is supported by the I.M. Rosenzweig Junior Investigator
493 Award from the Pulmonary Fibrosis Foundation. JRS is supported by the National Heart, Lung,
494 and Blood Institute (NHLBI – R01HL119215), by the NIAID Novel Alternative Model Systems for
495 Enteric Diseases (NAMSED) consortium (U19AI116482) and by grant number CZF2019-
496 002440 from the Chan Zuckerberg Initiative DAF, an advised fund of Silicon Valley Community
497 Foundation.

498 The authors would like to thank Matthew Chess for Amazon AWS support, Kevin Jan and
499 Peyton Uhl at Yokogawa for imaging support, Nick Santoro at the University of Michigan Center
500 for Chemical Genomics. We thank David Egan and Wienand Omta from Core Life Analytics for
501 assisting high content data analytics as well as Philip Cheung and Brian Bolt at ReFactor
502 Biosciences for assistance with HTS data registration. Finally, we thank Tracey Schultz and
503 Dianne Jazdzyk for project management.

504

505

506

507

508

509

510

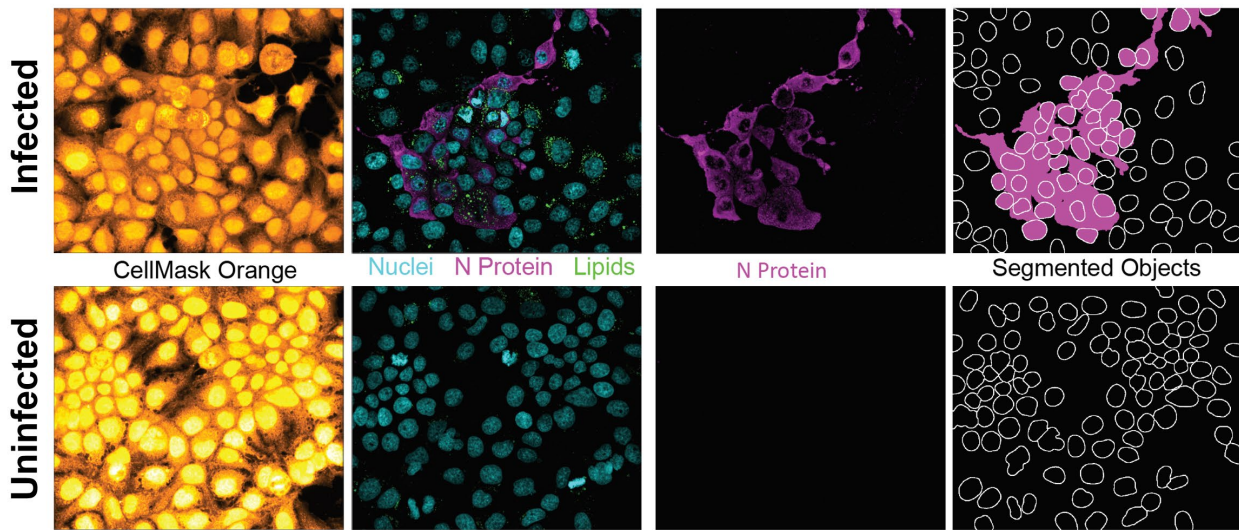
511

512

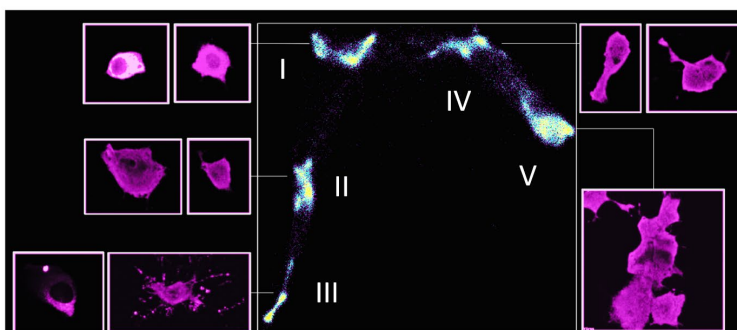
513 **FIGURES AND LEGENDS**

514

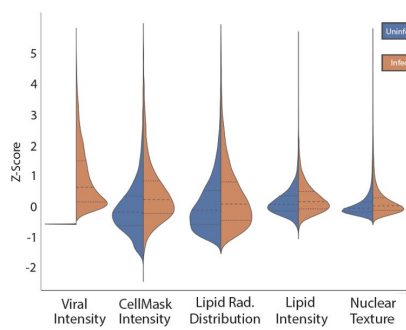
a



b



c



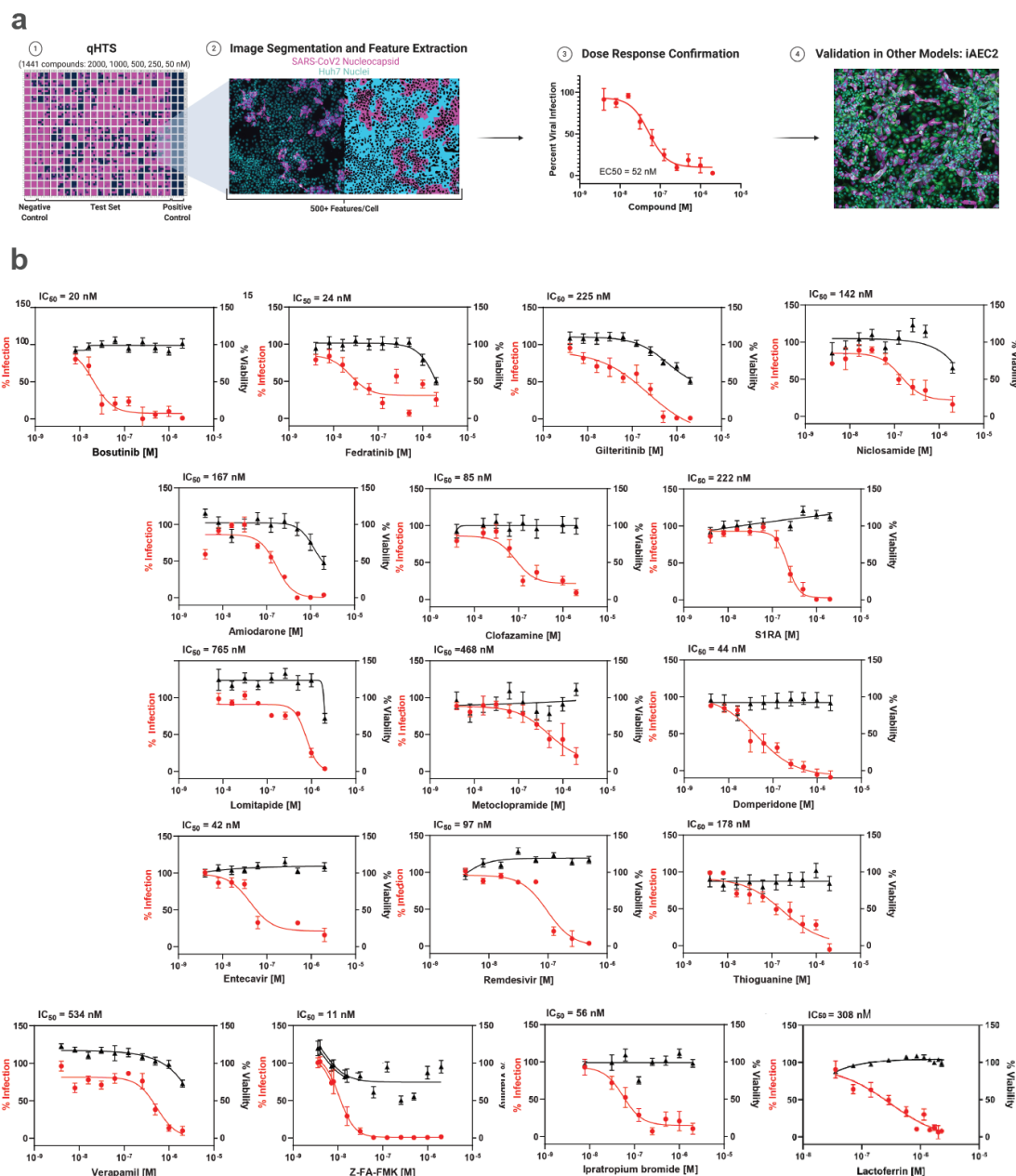
515

516

517 Figure 1. Morphological profiling of SARS-CoV-2 infected Huh7 cells (MOI of 0.2 for 48 hrs). A)
518 Clockwise: Representative field with nuclei (cyan), neutral lipids (green), and SARS-CoV-2 N
519 protein (magenta), N protein image in the same area with "fire" false color LUT showing distinct
520 morphologies of infected cells showing small/round cells with a hollow center, cells with
521 protrusions, and large syncytia, CellMask image showing cell boundaries and syncytia
522 formation. B) UMAP embedding and phenotypic clustering of 3 million cells showing distinct
523 morphologies present, including: small/bright cells (I), cells with protrusions (III), and syncytia
524 (V). C) Comparison of normalized cellular features in infected (brown) and uninfected (blue)
525 cells showing differences in cytoplasmic organization, lipid content/distribution and nuclear
526 texture. All distributions were compared with the Mann-Whitney test and are statistically
527 significant with $P < 0.0001$.

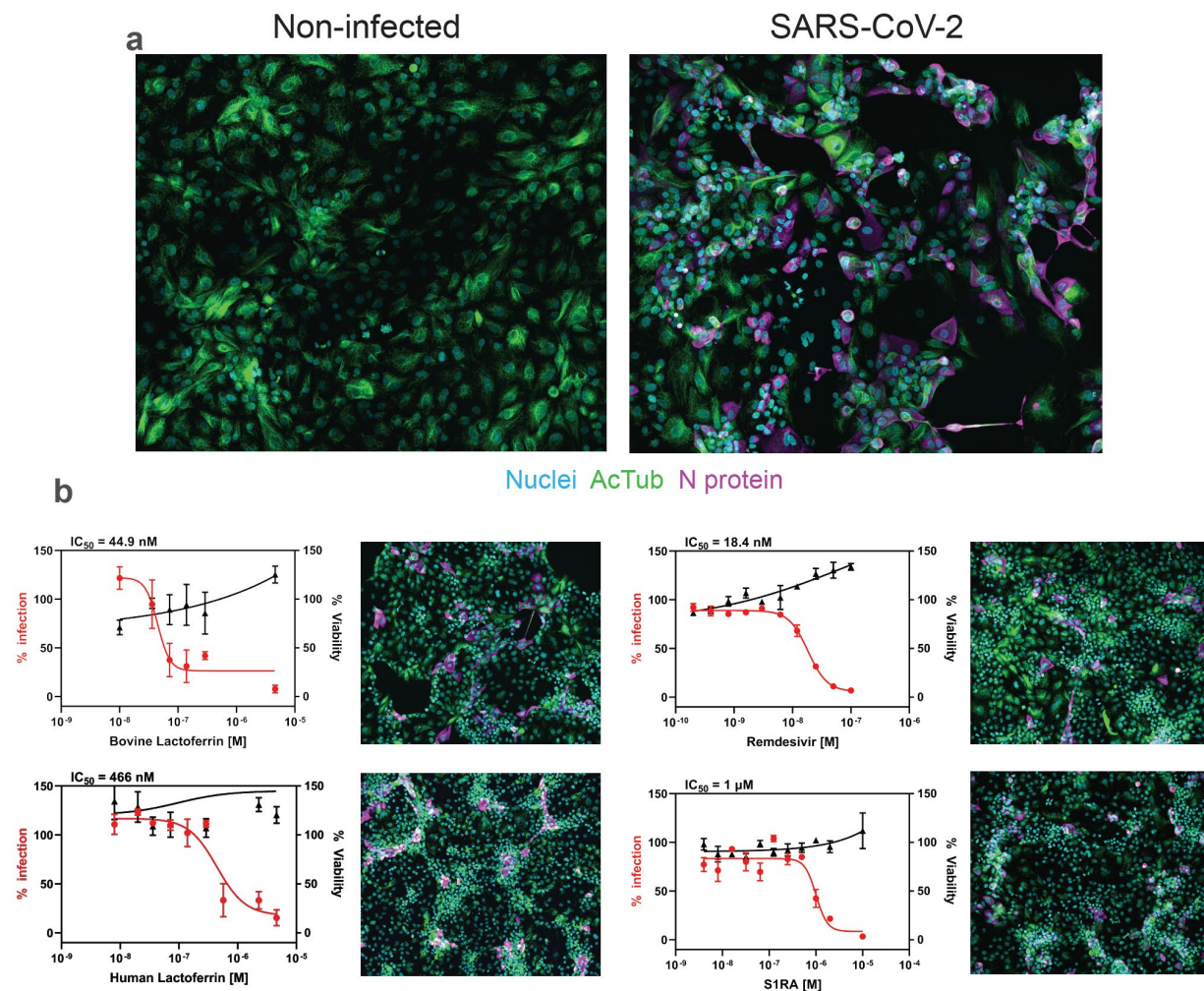
528

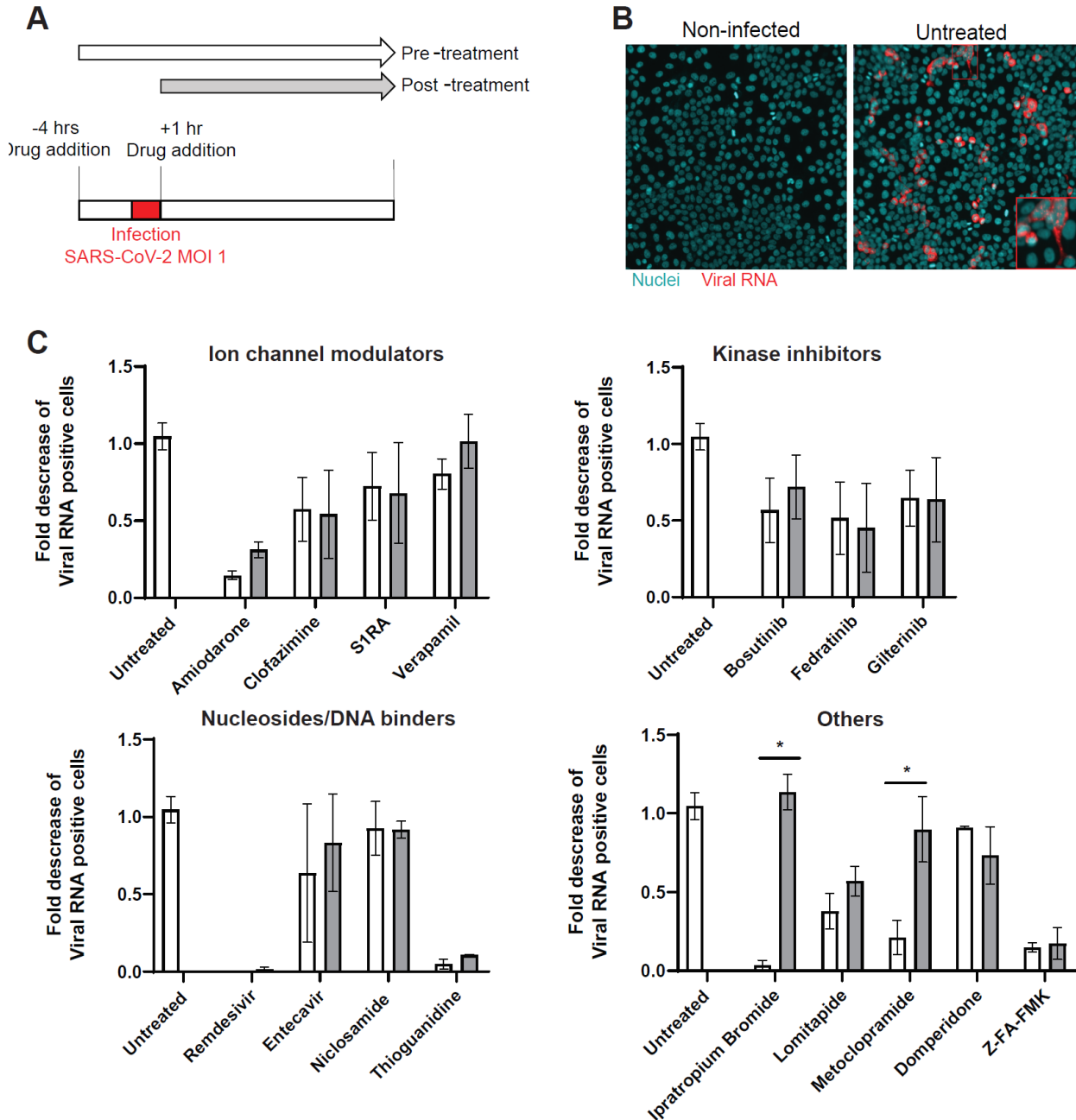
529



530
531

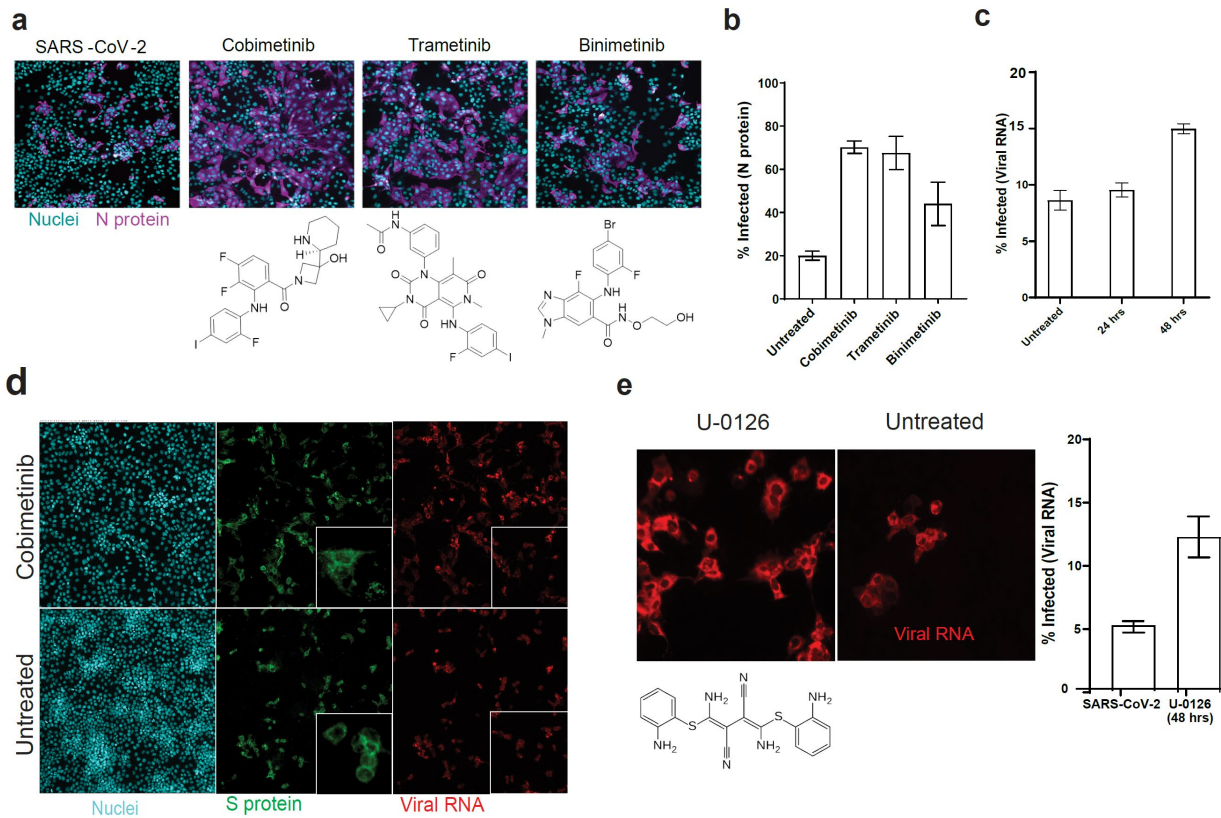
532 Figure 2. A) Schematic of the anti-SARS-CoV-2 drug repurposing screening. 1) Compounds are
533 administered in qHTS to cells cultured on 384-well plates infected with SARS-CoV-2 and
534 incubated for 48-hours. Each plate contains 32 negative (infected) and 32 positive (non-
535 infected) control wells. 2) Cells are fixed, stained, and imaged. Images are analyzed using Cell
536 Profiler to identify nuclei, cell boundaries, neutral lipid content and viral staining intensity. 3)
537 Dose-response curves are fit to normalized percent infected cells per well. 4) Confirmation of
538 antiviral activity in other cell lines, including a physiological relevant iPSC-derived human
539 alveolar epithelial cell (iAECs); B) Dose-response curves of 17 compounds. Graphs represent
540 median SEM of 10-point 1:2 dilution series of selected compounds for N=3 biological replicates.
541 IC₅₀ values were calculated based on normalization to the control and after fitting in GraphPad
542 Prism.





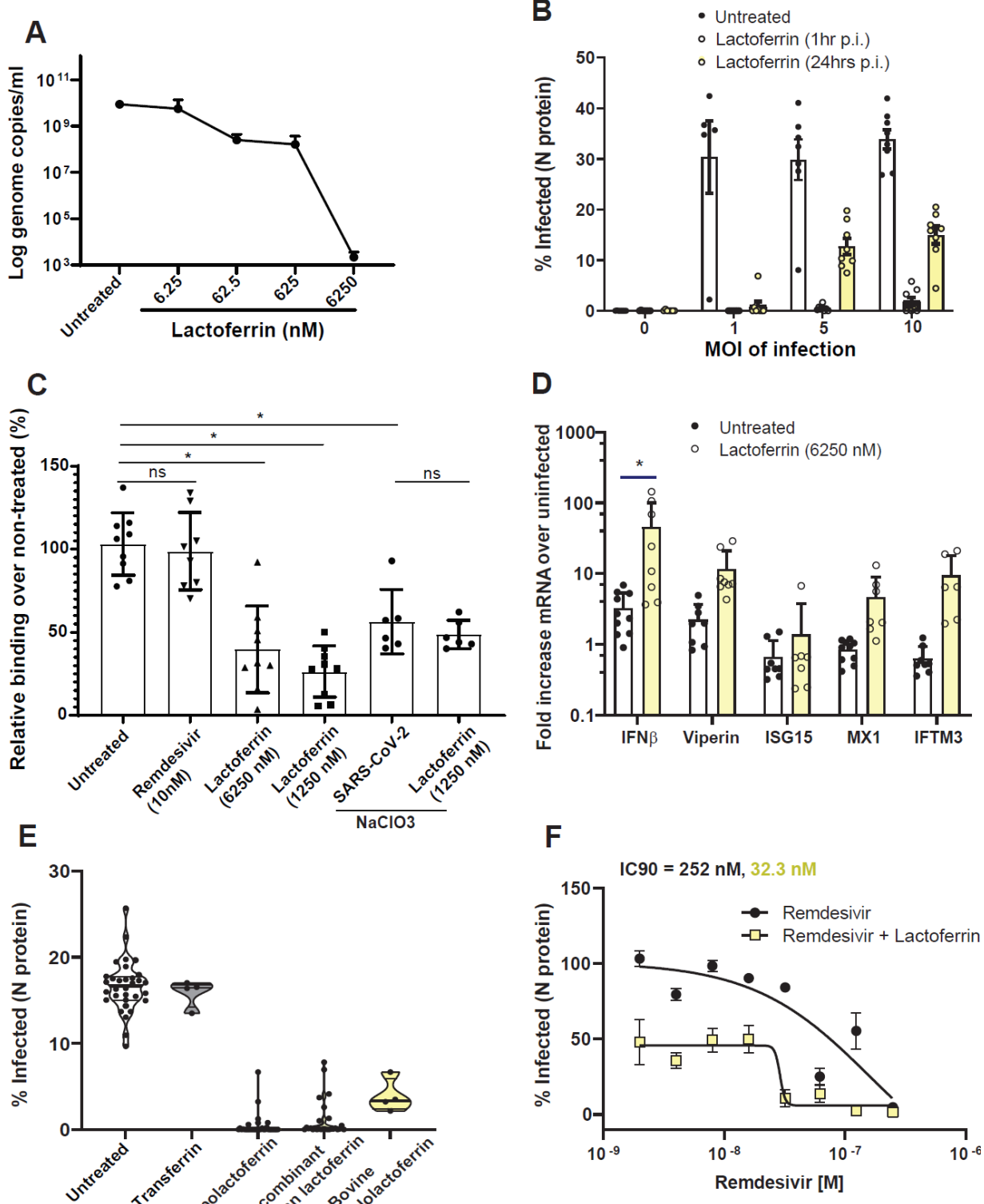
564
565
566
567
568
569
570
571
572
573
574
575
576

Figure 4. Time of drug-addition of the identified antiviral hits. A) Experimental scheme where compounds are added 4 hrs prior (same treatment window as drug screening) or 1 hr postinfection (p.i.) with SARS-CoV-2 (MOI of 1). Huh7 cells are fixed, permeabilized and subjected to RNAscope analysis 48 hrs p.i. B) Representative image of SARS-CoV-2 infected and non-infected Huh7 cells acquired on the CX5 high-content platform at 10X and analyzed with Fiji ImageJ. Viral RNA is represented in red, nuclei in cyan. C) Time of drug-addition for selected antiviral hits (at 10x IC₅₀ dose) organized according to the compound class. Graphs represent the fold decrease of infection over the untreated condition. Infection was calculated on the viral RNA image after image segmentation with Cell Profiler. Graphs represent an average SEM of N=3 biological replicates. Statistical significance determined using multiple student's t-test with the Bonferroni-Dunn correction method, with alpha = 0.05. *p<0.01.



577
578 Figure 5. Selective MEK inhibitors exacerbate SARS-CoV-2 infection. A) Representative images
579 of Huh7 cells infected with SARS-CoV-2 (MOI of 0.2) and treated with cobimetinib (250 nM),
580 trametinib (250 nM), and binimetinib (250 nM) with nuclei in cyan and N protein in magenta.
581 Viral infection was calculated on N protein images after image segmentation with Cell Profiler.
582 Bars represent N=3 technical replicates and unpaired t-tests with Welch's correction were
583 performed in Graphpad Prism. * p<0.001. B) RNAscope of Huh7 infected with SARS-CoV-2
584 (MOI of 1) treated with cobimetinib (1000 nM) and harvested at 24 hrs and 48 hrs p.i. Graph
585 represents average, SEM of N=3 biological replicates. D) Representative images of SARS-CoV-
586 2-infected (MOI of 1) and cobimetinib (1000 nM)-treated Huh7. Cells were harvested 48 hrs p.i.,
587 subjected to RNAscope to detect viral RNA (positive strand, in red) and counterstained with
588 anti-S protein antibody (green) and Hoechst 33342 (nuclei in cyan). E) SARS-CoV-2-infected
589 (MOI of 1) Huh7 were treated with U-0126 (10 μM) and subjected to RNAscope 48 hrs p.i.
590 Graph represents average SEM of N=2 biological replicates, each with three technical
591 replicates.

592
593
594
595
596
597
598
599
600
601
602



603
604
605
606
607

608
609 Figure 6. Lactoferrin blocks SARS-CoV-2 replication at different stages of the viral cycle. A)
610 Huh7 cells were infected with SARS-CoV-2 at MOI of 0.2 for 48 hrs and treated with increasing
611 concentration of lactoferrin (5.75 nM – 5750 nM). Cells were harvested and RNA was extracted.
612 Viral genome copies were calculated by RT-qPCR with an absolute quantification method. B)
613 Huh7 were infected with SARS-CoV-2 (MOI of 1, 5 and 10; MOI of 0 indicates non-infected
614 cells) and treated with 2.3 μ M of lactoferrin at 1 and 24 hrs p.i. Bars indicate the percentage of
615 infected cells in different conditions. Data is an average of eight replicates. Statistical
616 significance determined using multiple student's t-test with the Bonferroni-Dunn method, with
617 alpha = 0.05. Except for MOI of 0, all conditions (Untreated vs Lactoferrin, 1 hr or Untreated vs
618 Lactoferrin, 24 hr) differ by $p<0.0001$. C) Binding assay. Huh7 cells were pre-incubated on ice
619 with compounds: lactoferrin (100 μ g/mL and 500 μ g/mL) and remdesivir (10 nM), as a negative
620 control, for one hour and then infected with SARS-CoV-2 (MOI of 10) for 1h on ice. Cells were
621 then washed thoroughly with PBS to remove unbound virus and viral RNA was quantified by
622 RT-qPCR. Huh7 cultured in NaClO₃ for 7 days, which strips heparan sulfate proteoglycans from
623 the cell surface, were used as a control for lactoferrin mode of action. Data is shown after
624 normalization to viral control (100%) and represent an average of N=3 biological replicates with
625 N=2-3 technical replicates each. Unpaired t-tests with Welch's correction were performed in
626 Graphpad Prism to determine significance. * $p<0.0001$. D) mRNA levels of cellular IFN β , MX1,
627 ISG15 and IFITM3 were calculated with $\Delta\Delta Ct$ in SARS-CoV-2 infected and lactoferrin (5750
628 nM)-treated cells over uninfected Huh7. Data are average SD of N=2 biological replicates with
629 n=3 technical replicates each. Statistical significance was determined using multiple student's t-
630 test with the Bonferroni-Dunn method with alpha = 0.05. * $p<0.001$. E) Percentage of SARS-
631 CoV-2 infected Huh7 cells upon treatment with bovine apolactoferrin and hololactoferrin, native
632 human lactoferrin, and transferrin at a concentration of 2.3 μ M. F) Dose response of lactoferrin
633 (0 to 2.3 μ M) in combination with remdesivir (0 to 30 nM). Cells were pre-treated with
634 combination or single therapy and infected with SARS-CoV-2 (MOI of 0.2) for 48 hrs.
635
636
637
638
639
640
641
642
643
644
645
646
647
648
649
650
651
652
653
654
655
656
657
658

659 **Table 1: Compound Summary**

660

ID Drug Bank ID	Compound name	Indication	General mechanism of action	Potential mode of action against SARS-CoV2	IC50 (nM) Huh-7	IC50 (nM) Vero E6	IC50 (nM) Caco-2 E6	IC50 (nM) LNcaP E6	IC50 (nM) iAEC2
DB01118	Amiodarone (hydrochloride)	Treatment of ventricular tachycardia	Inhibitor of K and Ca channels	Entry inhibitor Evaluated in clinical trial for COVID19 (NCT04351763)	167	1406	5500	>5000	118
DB06616	Bosutinib	Treatment of chronic myeloid leukemia	Bcr-Abl kinase inhibitor	Inhibitor of S protein fusion similar to the related Imatinib	20	>5000	IA	Inverse	IA
DB00845	Clofazimine	Treatment of leprosy	Binds to mycobacterial DNA and K transporters inhibitor	Entry inhibitor Evaluated in clinical trial for COVID19 (NCT04465695)	85	>5000	>5000	29	>5000
DB01184	Domperidone	Antiemetic	Dopamine D2 receptor antagonist	Host modulation	44	IA	IA	ND	IA
DB00442	Entecavir (hydrate)	Treatment of hepatitis B virus	Transcription inhibitor, nucleoside analog	Replication inhibitor	42	>5000	IA	IA	IA
DB12500	Fedratinib	Treatment of intermediate-2 and high risk primary and secondary myelofibrosis	Tyrosine kinase inhibitor (Jak1)	Predicted inhibitor of kinase (NAK) family reported to reduce viral infection in vitro. Reduction of TH17 responses responsible of SARS-CoV-2 associated cytokine storm	24	>5000	>5000	>5000	1810
DB12141	Gilteritinib	Treatment of FLT3-mutated acute myeloid leukemia (AML)	FMS-like tyrosine kinase 3 (FLT3) inhibitor	Host modulation	225	2344	IA	IA	>5000
DB00332	Ipratropium Bromide	Treatment of COPD and asthma	Muscarinic receptor antagonist	Binding inhibitor	56	NA	85	>5000	4
NA	Lactoferrin	Diet supplement	Iron chelator, immune-modulator Antimicrobial activity	Entry and post-entry inhibitor	308	NA	1170	157	45
DB08827	Lomitapide	Treatment of homozygous familial hypercholesterolemia	Microsomal triglyceride transfer protein (MTP) inhibitor	Host lipid metabolism modulation	765	1875	>5000	IA	733
DB01233	Metoclopramide	Treatment of diabetic gastroparesis	Dopamine D2 and serotonin 5-HT3 receptor inhibitor	Binding inhibitor	468	>5000	IA	IA	IA
DB06803	Niclosamide	Treatment of tapeworm infections	Mitochondrial uncoupler, mTORC1 inhibitor	Autophagy and endocytic pathway inhibitor	142	>5000	IA	>5000	NA
DB14761	Remdesivir	Investigational for Ebola virus treatment	Transcription inhibitor, nucleoside analog	Replication inhibitor Emergency FDA approval for COVID19	97	NA	19	106	18
ZINC95000617	S1RA	Treatment of neuropathic pain (phase II)	Sigma R1/R2 modulator	Entry inhibitor	222	>5000	>5000	IA	1
DB00352	Thioguanine	Therapy of acute leukemia	Guanine analogue	Replication inhibitor	178	820	674	29	IA
DB00661	Verapamil (hydrochloride)	Treatment of high blood pressure, heart arrhythmias, and anginaT	Ca channel inhibitor	Entry inhibitor Evaluated in clinical trial for COVID19 (NCT04351763)	534	>5000	Low	18	NA
CAS 197855-65-5	Z-FA-FMK	Preclinical	Irreversible inhibitor of cysteine proteases (cathepsin L)	Entry inhibitor	11	51	Low	514	4

661

662

663 NA=not tested, IA-inactive, >5000 indicates activity but loss of potency, Low=IC50 below 1nM.
 664 Grey rows indicate compounds with efficacy across multiple cell systems.

665

666

667

668

669

670

671

672

673

674

675

676

677

678

679

680

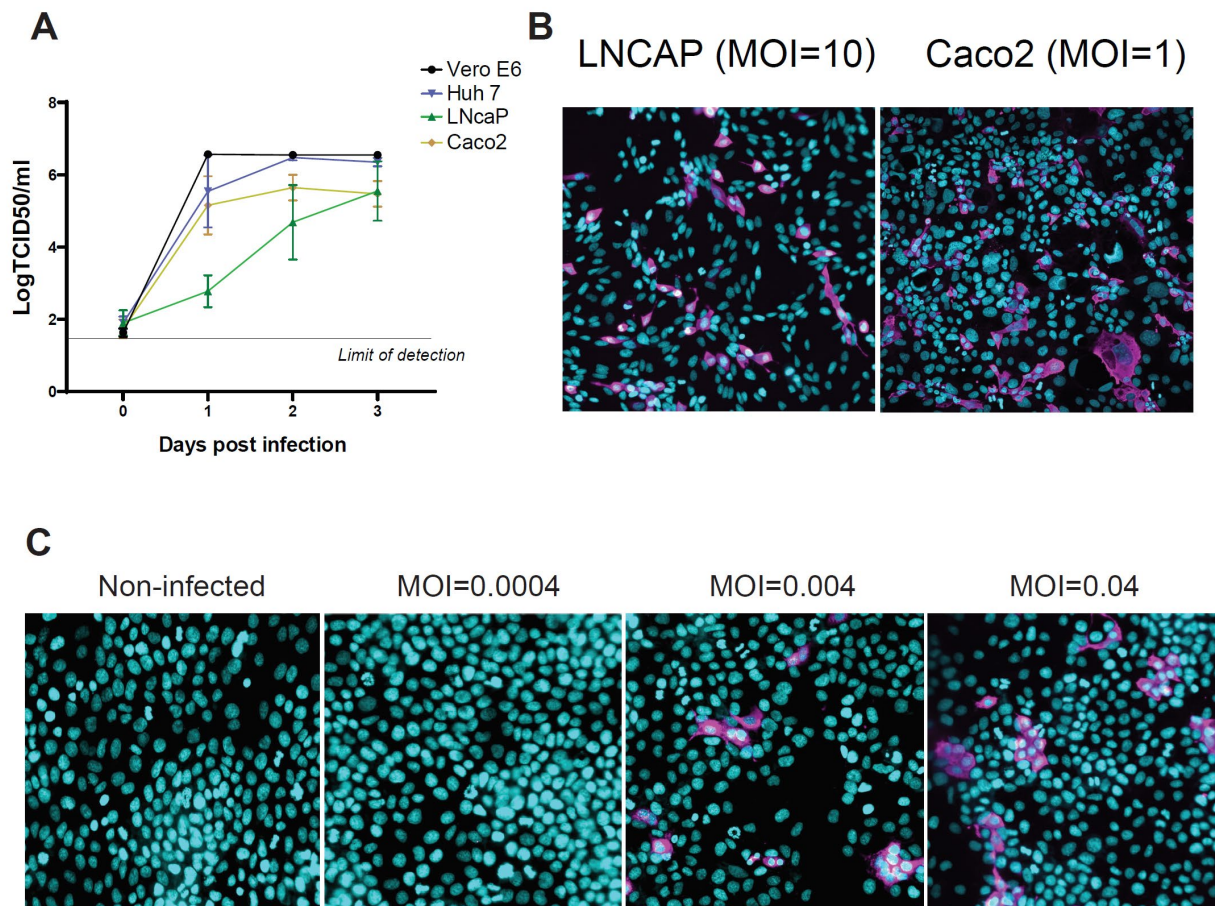
681

682

683

684

685 **SUPPLEMENTARY INFORMATION**



686

687 **Supplementary Figure 1:** a) Growth kinetics of Vero E6, Huh-7 and Caco-2 cells. Cells were
688 infected in 48-well plates with SARS-CoV-2 at an MOI of 0.2 and harvested at day 0 (1h post
689 adsorption), day 1, 2 and 3. TCID₅₀ determination was performed on the supernatant and cellular
690 fraction. Graph represents median, SD of N=2 biological replicates with n=3 technical replicate
691 each. B) Syncytia formation (magenta, anti-SARS-CoV-2 N antibody) in SARS-CoV-2 infected
692 Vero E6 (left) and Caco2 (right) cells counter stained with Hoechst 33342 (cyan) and anti-SARS-
693 CoV-2 N antibody (magenta).[\[cW1\]](#) C) Limit of detection of the assay. Huh-7 cells were infected at
694 indicated MOI and imaged at 48h p.i. Progressive and more feature-rich syncytia formation was
695 observed in correlation with an increased MOI and detection was possible with infection as low
696 as MOI 0.004.

697

698

699

700 **REFERENCES**

701

- 702 1. Xiao F, Tang M, Zheng X, Liu Y, Li X, Shan H. 2020. Evidence for Gastrointestinal Infection of SARS-CoV-2. *Gastroenterology*.
- 704 2. Lin L, Jiang X, Zhang Z, Huang S, Zhang Z, Fang Z, Gu Z, Gao L, Shi H, Mai L, Liu Y, Lin X, Lai R, Yan Z, Li X, Shan H. 2020. Gastrointestinal symptoms of 95 cases with SARS-CoV-2 infection. *Gut* 69:997–1001.
- 707 3. Avula A, Nalleballe K, Narula N, Sapozhnikov S, Dandu V, Toom S, Glaser A, Elsayegh D. 2020. COVID-19 presenting as stroke. *Brain Behav Immun* <https://doi.org/10.1016/j.bbi.2020.04.077>.
- 709 4. Kochi AN, Tagliari AP, Forleo GB, Fassini GM, Tondo C. 2020. Cardiac and arrhythmic complications in patients with COVID-19. *J Cardiovasc Electrophysiol* 31:1003–1008.
- 711 5. Mulangu S, Dodd LE, Davey RT Jr, Tshiani Mbaya O, Proschan M, Mukadi D, Lusakibanza Manzo M, Nzolo D, Tshomba Oloma A, Ibanda A, Ali R, Coulibaly S, Levine AC, Grais R, Diaz J, Lane HC, Muyembe-Tamfum J-J, PALM Writing Group, Sivahera B, Camara M, Kojan R, Walker R, Dighero-Kemp B, Cao H, Mukumbayi P, Mbala-Kingebeni P, Ahuka S, Albert S, Bonnett T, Crozier I, Duvenhage M, Proffitt C, Teitelbaum M, Moench T, Aboulhab J, Barrett K, Cahill K, Cone K, Eckes R, Hensley L, Herpin B, Higgs E, Ledgerwood J, Pierson J, Smolskis M, Sow Y, Tierney J, Sivapalasingam S, Holman W, Gettinger N, Vallée D, Nordwall J, PALM Consortium Study Team. 2019. A Randomized, Controlled Trial of Ebola Virus Disease Therapeutics. *N Engl J Med* 381:2293–2303.
- 719 6. Oprea TI, Bauman JE, Bologa CG, Buranda T, Chigaev A, Edwards BS, Jarvik JW, Gresham HD, Haynes MK, Hjelle B, Hromas R, Hudson L, Mackenzie DA, Muller CY, Reed JC, Simons PC, Smagley Y, Strouse J, Surviladze Z, Thompson T, Ursu O, Waller A, Wandinger-Ness A, Winter SS, Wu Y, Young SM, Larson RS, Willman C, Sklar LA. 2011. Drug Repurposing from an Academic Perspective. *Drug Discov Today Ther Strateg* 8:61–69.
- 724 7. McQuin C, Goodman A, Chernyshev V, Kamentsky L, Cimini BA, Karhohs KW, Doan M, Ding L, Rafelski SM, Thirstrup D, Wiegraebe W, Singh S, Becker T, Caicedo JC, Carpenter AE. 2018. CellProfiler 3.0: Next-generation image processing for biology. *PLoS Biol* 16:e2005970.
- 727 8. Chen W, Li X-M, Li A-L, Yang G, Hu H-N. 2016. Hepatitis C Virus Increases Free Fatty Acids Absorption and Promotes its Replication Via Down-Regulating GADD45 α Expression. *Med Sci Monit* 22:2347–2356.
- 730 9. Riva L, Yuan S, Yin X, Martin-Sancho L, Matsunaga N, Pache L, Burgstaller-Muehlbacher S, De Jesus PD, Teriete P, Hull MV, Chang MW, Chan JF-W, Cao J, Poon VK-M, Herbert KM, Cheng K, Nguyen T-TH, Rubanov A, Pu Y, Nguyen C, Choi A, Rathnasinghe R, Schotsaert M, Miorin L, Dejosez M, Zwaka TP, Sit K-Y, Martinez-Sobrido L, Liu W-C, White KM, Chapman ME, Lendy EK, Glynne RJ, Albrecht R, Ruppin E, Mesecar AD, Johnson JR, Benner C, Sun R, Schultz PG, Su AI, García-Sastre A, Chatterjee AK, Yuen K-Y, Chanda SK. 2020. Discovery of SARS-CoV-2 antiviral drugs through large-scale compound repurposing. *Nature* 586:113–119.

- 737 10. Heiser K, McLean PF, Davis CT, Fogelson B, Gordon HB, Jacobson P, Hurst B, Miller B, Alfa RW,
738 Earnshaw BA, Victors ML, Chong YT, Haque IS, Low AS, Gibson CC. 2020. Identification of potential
739 treatments for COVID-19 through artificial intelligence-enabled phenomic analysis of human cells
740 infected with SARS-CoV-2. *bioRxiv*.
- 741 11. Jeon S, Ko M, Lee J, Choi I, Byun SY, Park S, Shum D, Kim S. Identification of antiviral drug
742 candidates against SARS-CoV-2 from FDA-approved drugs.
- 743 12. Yang L, Pei R-J, Li H, Ma X-N, Zhou Y, Zhu F-H, He P-L, Tang W, Zhang Y-C, Xiong J, Xiao S-Q, Tong X-
744 K, Zhang B, Zuo J-P. 2020. Identification of SARS-CoV-2 entry inhibitors among already approved
745 drugs. *Acta Pharmacol Sin* <https://doi.org/10.1038/s41401-020-00556-6>.
- 746 13. Hurley K, Ding J, Villacorta-Martin C, Herriges MJ, Jacob A, Vedaie M, Alyandratos KD, Sun YL, Lin C,
747 Werder RB, Huang J, Wilson AA, Mithal A, Mostoslavsky G, Oglesby I, Caballero IS, Guttentag SH,
748 Ahangari F, Kaminski N, Rodriguez-Fraticelli A, Camargo F, Bar-Joseph Z, Kotton DN. 2020.
749 Reconstructed Single-Cell Fate Trajectories Define Lineage Plasticity Windows during Differentiation
750 of Human PSC-Derived Distal Lung Progenitors. *Cell Stem Cell* 26:593–608.e8.
- 751 14. Mason RJ. 2020. Pathogenesis of COVID-19 from a cell biology perspective. *Eur Respir J* 55.
- 752 15. Lang J, Yang N, Deng J, Liu K, Yang P, Zhang G, Jiang C. 2011. Inhibition of SARS pseudovirus cell
753 entry by lactoferrin binding to heparan sulfate proteoglycans. *PLoS One* 6:e23710.
- 754 16. Kell DB, Heyden EL, Pretorius E. 2020. The Biology of Lactoferrin, an Iron-Binding Protein That Can
755 Help Defend Against Viruses and Bacteria. *Front Immunol* 11:1221.
- 756 17. Baeuerle PA, Huttner WB. 1986. Chlorate — a potent inhibitor of protein sulfation in intact cells.
757 Biochemical and Biophysical Research Communications.
- 758 18. Siqueiros-Cendón T, Arévalo-Gallegos S, Iglesias-Figueroa BF, García-Montoya IA, Salazar-Martínez
759 J, Rascón-Cruz Q. 2014. Immunomodulatory effects of lactoferrin. *Acta Pharmacol Sin* 35:557–566.
- 760 19. Blanco-Melo D, Nilsson-Payant BE, Liu W-C, Uhl S, Hoagland D, Møller R, Jordan TX, Oishi K, Panis
761 M, Sachs D, Wang TT, Schwartz RE, Lim JK, Albrecht RA, tenOever BR. 2020. Imbalanced Host
762 Response to SARS-CoV-2 Drives Development of COVID-19. *Cell* 181:1036–1045.e9.
- 763 20. Kuleshov MV, Stein DJ, Clarke DJB, Kropiwnicki E, Jagodnik KM, Bartal A, Evangelista JE, Hom J,
764 Cheng M, Bailey A, Zhou A, Ferguson LB, Lachmann A, Ma'ayan A. 2020. The COVID-19 Drug and
765 Gene Set Library. Patterns.
- 766 21. Yin W, Mao C, Luan X, Shen D-D, Shen Q, Su H, Wang X, Zhou F, Zhao W, Gao M, Chang S, Xie Y-C,
767 Tian G, Jiang H-W, Tao S-C, Shen J, Jiang Y, Jiang H, Xu Y, Zhang S, Zhang Y, Xu HE. 2020. Structural
768 basis for inhibition of the RNA-dependent RNA polymerase from SARS-CoV-2 by remdesivir. *Science*
769 368:1499–1504.
- 770 22. Ghahremanpour MM, Tirado-Rives J, Deshmukh M, Ippolito JA, Zhang C-H, de Vaca IC, Liosi M-E,
771 Anderson KS, Jorgensen WL. Identification of 14 Known Drugs as Inhibitors of the Main Protease of
772 SARS-CoV-2.

- 773 23. Roscow O, Ganassin R, Garver K, Polinski M. 2018. Z-FA-FMK demonstrates differential inhibition of
774 aquatic orthoreovirus (PRV), aquareovirus (CSRV), and rhabdovirus (IHNV) replication. *Virus Res*
775 244:194–198.
- 776 24. Ou X, Liu Y, Lei X, Li P, Mi D, Ren L, Guo L, Guo R, Chen T, Hu J, Xiang Z, Mu Z, Chen X, Chen J, Hu K,
777 Jin Q, Wang J, Qian Z. 2020. Characterization of spike glycoprotein of SARS-CoV-2 on virus entry and
778 its immune cross-reactivity with SARS-CoV. *Nat Commun* 11:1620.
- 779 25. Pardanani A, Hood J, Lasho T, Levine RL, Martin MB, Noronha G, Finke C, Mak CC, Mesa R, Zhu H,
780 Others. 2007. TG101209, a small molecule JAK2-selective kinase inhibitor potently inhibits
781 myeloproliferative disorder-associated JAK2 V617F and MPL W515L/K mutations. *Leukemia*
782 21:1658–1668.
- 783 26. Wu D, Yang XO. 2020. TH17 responses in cytokine storm of COVID-19: An emerging target of JAK2
784 inhibitor Fedratinib. *J Microbiol Immunol Infect* <https://doi.org/10.1016/j.jmii.2020.03.005>.
- 785 27. Zhang W, Zhao Y, Zhang F, Wang Q, Li T, Liu Z, Wang J, Qin Y, Zhang X, Yan X, Zeng X, Zhang S. 2020.
786 The use of anti-inflammatory drugs in the treatment of people with severe coronavirus disease
787 2019 (COVID-19): The Perspectives of clinical immunologists from China. *Clinical Immunology*.
- 788 28. Stebbing J, Phelan A, Griffin I, Tucker C, Oechsle O, Smith D, Richardson P. 2020. COVID-19:
789 combining antiviral and anti-inflammatory treatments. *Lancet Infect Dis*. thelancet.com.
- 790 29. Treatment of Moderate to Severe Coronavirus Disease (COVID-19) in Hospitalized Patients - Full
791 Text View - ClinicalTrials.gov.
- 792 30. Cai Y, Liu Y, Zhang X. 2007. Suppression of coronavirus replication by inhibition of the MEK signaling
793 pathway. *J Virol* 81:446–456.
- 794 31. Gu J, Han B, Wang J. 2020. COVID-19: gastrointestinal manifestations and potential fecal--oral
795 transmission. *Gastroenterology* 158:1518–1519.
- 796 32. Reghunathan R, Jayapal M, Hsu L-Y, Chng H-H, Tai D, Leung BP, Melendez AJ. 2005. Expression
797 profile of immune response genes in patients with Severe Acute Respiratory Syndrome. *BMC
798 Immunol* 6:2.
- 799 33. Han C, Duan C, Zhang S, Spiegel B, Shi H, Wang W, Zhang L, Lin R, Liu J, Ding Z, Hou X. 2020.
800 Digestive Symptoms in COVID-19 Patients With Mild Disease Severity: Clinical Presentation, Stool
801 Viral RNA Testing, and Outcomes. *Am J Gastroenterol*
802 <https://doi.org/10.14309/ajg.00000000000000664>.
- 803 34. Oda H, Kolawole AO, Mirabelli C, Wakabayashi H, Tanaka M, Yamauchi K, Abe F, Wobus CE. 2020.
804 Antiviral Effects of Bovine Lactoferrin on Human Norovirus. *Biochem Cell Biol*
805 <https://doi.org/10.1139/bcb-2020-0035>.
- 806 35. Cutone A, Frioni A, Berlutti F, Valenti P, Musci G, Bonaccorsi di Patti MC. 2014. Lactoferrin prevents
807 LPS-induced decrease of the iron exporter ferroportin in human monocytes/macrophages.
808 *Biometals* 27:807–813.

- 809 36. Conti P, Ronconi G, Caraffa A, Gallenga C, Ross R, Frydas I, Kritas S. 2020. Induction of pro-
810 inflammatory cytokines (IL-1 and IL-6) and lung inflammation by Coronavirus-19 (COVI-19 or SARS-
811 CoV-2): anti-inflammatory strategies. *J Biol Regul Homeost Agents* 34.
- 812 37. Lagunas-Rangel FA, Chávez-Valencia V. 2020. High IL-6/IFN- γ ratio could be associated with severe
813 disease in COVID-19 patients. *J Med Virol* <https://doi.org/10.1002/jmv.25900>.
- 814 38. Hung IF-N, Lung K-C, Tso EY-K, Liu R, Chung TW-H, Chu M-Y, Ng Y-Y, Lo J, Chan J, Tam AR, Shum H-P,
815 Chan V, Wu AK-L, Sin K-M, Leung W-S, Law W-L, Lung DC, Sin S, Yeung P, Yip CC-Y, Zhang RR, Fung
816 AY-F, Yan EY-W, Leung K-H, Ip JD, Chu AW-H, Chan W-M, Ng AC-K, Lee R, Fung K, Yeung A, Wu T-C,
817 Chan JW-M, Yan W-W, Chan W-M, Chan JF-W, Lie AK-W, Tsang OT-Y, Cheng VC-C, Que T-L, Lau C-S,
818 Chan K-H, To KK-W, Yuen K-Y. 2020. Triple combination of interferon beta-1b, lopinavir–ritonavir,
819 and ribavirin in the treatment of patients admitted to hospital with COVID-19: an open-label,
820 randomised, phase 2 trial. *Lancet* [https://doi.org/10.1016/S0140-6736\(20\)31042-4](https://doi.org/10.1016/S0140-6736(20)31042-4).
- 821 39. Jacob A, Morley M, Hawkins F, McCauley KB, Jean JC, Heins H, Na C-L, Weaver TE, Vedaie M, Hurley
822 K, Hinds A, Russo SJ, Kook S, Zacharias W, Ochs M, Traber K, Quinton LJ, Crane A, Davis BR, White
823 FV, Wambach J, Whitsett JA, Cole FS, Morrisey EE, Guttentag SH, Beers MF, Kotton DN. 2017.
824 Differentiation of Human Pluripotent Stem Cells into Functional Lung Alveolar Epithelial Cells. *Cell*
825 *Stem Cell* 21:472–488.e10.
- 826 40. Berthold MR, Cebron N, Dill F, Gabriel TR, Kötter T, Meinl T, Ohl P, Thiel K, Wiswedel B. 2009.
827 KNIME - the Konstanz information miner. *ACM SIGKDD Explorations Newsletter*.
- 828 41. McInnes L, Healy J, Melville J. 2018. UMAP: Uniform Manifold Approximation and Projection for
829 Dimension Reduction. *arXiv [statML]*.
- 830 42. Stevens J-LR, Rudiger P, Bednar JA. 2015. HoloViews: Building complex visualizations easily for
831 reproducible science, p. 61–69. In *Proceedings of the 14th Python in Science Conference*.